

Effects of Geometric Modelling and Blood Rheology in Patient-Specific Arterial Blood Flow Simulations with Speed-Accuracy Trade-Off Analysis

Rishi Kumar¹, K. Muralidhar^{2*}, and Indranil Saha Dalal^{1*}

¹Department of Chemical Engineering, Indian Institute of Technology, Kanpur, India 208016

²Department of Mechanical Engineering, Indian Institute of Technology, Kanpur, India 208016

Abstract

This study investigates the effects of geometry modeling and reduction on predictions of blood flow in patient-specific descending aorta obtained from Computed Tomography (CT) scan data, followed by speed-accuracy trade-off analysis using 3D simulations. Additionally, we show how wall shear stresses (WSS) can be estimated for such realistic arteries using cheaper simulations of highly idealized equivalent geometries. The study uses realistic inflow (with mean $Re = 313.6$ and peak $Re = 1687$ based on Newtonian viscosity) and pressure outlet boundary conditions with Newtonian and non-Newtonian blood viscosity models, including the one developed by Apostolidis and Beris [Alex J Apostolidis and Antony N Beris. "Modeling of the blood rheology in steady-state shear flows", *Journal of Rheology*, 58(3):607–633, (2014)]. Similar studies exist to predict the progression of atherosclerosis, clots, aneurysms and thrombus formation in arteries. However, these assume idealized flow geometries. In contrast, real arteries possess significant amounts of roughness, perturbations, and undulations. To understand their impact along with blood rheology, studies are performed with two levels of geometry reduction. Our results show the effects of such simplifications on flow field predictions in conjunction with blood rheology models. The first level of reduction loses the local asymmetry but is

able to reasonably approximate various parameters, capturing patterns with the correct magnitude while showing significant computational speed-up. However, further simplification to an idealized smooth geometry loses all information about the vortex structures in the flow field. The flow recirculation zones near wall perturbations progressively weaken as the geometry is smoothed. Broadly, for blood rheology models, no significant differences are observed between the various types used in this study. Interestingly, for all models, the idealized smooth geometry, combined with area correction, yields WSS estimates that closely approximate those of the actual artery. In this study, we also present a detailed speed-accuracy trade-off analysis useful for future applications. The number of iterations to convergence becomes progressively lower with geometry reduction, with nearly four times speed-up obtained with the first level of simplification. Further, the computational time for the Newtonian model remains approximately an order of magnitude lower than the non-Newtonian counterparts.

Keywords— blood flow, descending aorta, geometry perturbations, pulsatile waveform, wall shear stress

1 Introduction

Cardiovascular diseases (CVD) remain one primary reason for human mortality [1] and have grown in importance after the COVID-19 pandemic. The progression of CVD is directly related to the geometric details of the arteries [2]. CVD is known to aggravate other conditions as well [3]. Over the last few decades, greater computing power has enabled detailed computational studies on blood flow in the human arteries [4, 5]. Researchers have been interested in the link between atherosclerosis and fluid flow and related parameters, including the wall shear stress (WSS) [6–9]. Increasingly, studies have used patient-specific geometries with the aim of contributing to medical applications [10]. Similar studies have been reported to predict the progression

of atherosclerosis [11, 12], clots [13], aortic aneurysm [14] and formation of thrombus [15]. Significant studies have investigated the effect of stenosis on blood flow [16–19]. However, in all these studies, the flow geometries have been assumed to be quite regular. In contrast, human arteries are far from regular and possess a significant amount of undulations in diameter as well as in the flow direction. The geometrical variations of arteries have been linked to the onset of atherosclerosis [20–22], thereby justifying its importance in the broader aspect of human health.

Despite the importance of irregularities in geometry, researchers have rarely focused on their impact on blood flow. Yi et al. [23] performed simulations to study the impact of surface roughness on arterial stenosis. Shukla et al. [24] studied the effect of surface roughness on pulsatile flow in a tube with a periodic pattern of roughness in the form of sinusoids while Owen et al. [25] studied the effect of surface roughness on blood flow in a tube. To the best of our knowledge, these three studies come closest to the studying the impact of roughness from a biological perspective for blood flow analysis. Among them, the studies by Yi et al. [23] and Shukla et al. [24] use Newtonian fluid models. Owen et al. [25] used a variety of models, including Newtonian and non-Newtonian ones, to study the effect of an uneven geometry. However, the geometry and setup they created in the study can be argued to be far removed from reality. In a tube, they made a "rough" patch with surface irregularities that extended along the length and compared fluid flow results between the rough patch and an equivalent smooth patch on the other side. This geometrical setup has two significant problems. Firstly, the roughness is distributed all over the surface, and a tube with a rough and smooth patch is not close to the surface features of arteries in our body. Secondly, the surface features comprise not just roughness but also changes on the scale of the artery diameter. Hence, irregularities also exist in the shape and size fluctuations along the axial length of the arterial tube. The flowing fluid experiences the combined effect of these irregularities. As discussed later, the real artery may deviate significantly from the circular shape over a given plane. Additionally, the equivalent diameter can also show variations along the axis. To the best of our knowledge, no previous study has investigated the effect of

such shape and size perturbations, in addition to surface roughness, which is aimed for in the present study. Also, we use a variety of viscosity models to examine the sensitivity of the non-Newtonian nature of blood with geometric perturbations.

Thus, in this study, we start with a patient-specific geometry – a part of the descending aorta with all possible details and perturbations retained for blood flow calculations. To mimic real-life conditions, we use a variety of viscosity models and realistic pulsatile inflow and pressure outlet boundary conditions. Recent developments in computational fluid dynamics have enabled blood flow studies in realistic arterial geometries. Thus, it is possible to compute flow distribution in three dimensions for pulsatile flow in branches and bifurcations with bulges and constrictions. When the geometry is made realistic, undulations and perturbations of the artery wall need refinement in mesh size, thereby increasing computational cost. Secondly, for an accurate representation of a complex fluid such as blood, non-Newtonian rheology models need to be used, further increasing complexity. In the present study, we explore the consequences of simplifying the geometry in the context of various viscosity models (with an additional aim of reducing computational cost). The original artery model is obtained from CT scans, and progressively simpler geometries are generated by smoothing operations in image processing. We study hemodynamic aspects using Newtonian and non-Newtonian viscosity models in these equivalent geometries. Further, comparisons of results across these different geometries can yield insights into the importance of geometric resolution and perturbations on the flow field.

Towards this goal, three levels of equivalent geometries are studied. Level 1 is the original geometry derived from DICOM images provided by a medical hospital. Level 2 represents the same artery, divided into slices along its length, each slice representing a smooth duct of constant diameter. The number of slices can be varied to create varying levels of overall “smoothness”. Level 3 is a straight, smooth, circular tube of linearly varying diameter whose inlet and outlet diameters match the original. Inlet flow waveform is specified in terms of the peak flow rate and frequency. The significance of the outcome of this study

is manifold. The most direct one is linked to medical measurements and device points of view. Alternatively, the study provides us with an understanding of the modeling aspects required for a given level of resolution of the selected artery. If we need to perform CFD calculations on an arterial geometry, the question of interest is, will a simplified geometry be sufficient? Or will the actual geometry with all small-scale details be needed to obtain medically relevant results? In addition, such studies also reveal the speed-accuracy trade-off. It is expected that the simplified geometric representation can be simulated in a lesser amount of computational time. However, some information is bound to be lost in the process of geometric simplification. For a particular application, one needs to anticipate the compromise in geometry permitted to perform a sufficiently accurate calculation in as little time as possible. This question is addressed in the present study by adopting equivalent geometries as described earlier.

One additional aspect studied here is the change obtained by the choice of the viscosity model. Calculations in these three equivalent geometric representations provide intricate details of the effects of geometric perturbations on the flow of blood and their connection with the chosen rheological model, apart from the effect of these details on the computational speed. Additionally, we also ask an inverse question. Since highly idealized geometries are computationally cheaper, is it possible to use such simulations to obtain an estimate of relevant haemodynamic parameters in the patient-specific, real geometry with all perturbations and undulations? In this study, we show the feasibility of this aspect for estimating WSS, which is extremely relevant in medical fields. The close agreement of such estimates and simulation results on the actual geometry, particularly for non-Newtonian models, opens up further possibilities for future applications.

The outcomes of the simulations are shown in terms of vortical patterns and hemodynamic parameters such as the time average wall shear stress (TAWSS) and oscillatory shear index (OSI). The accuracy losses are shown in terms of correlations defined in the article, which provides a numerical estimate of the loss of prediction accuracy across various simplification levels. The differences in flow patterns among the three levels are discussed in detail, with

an understanding of the substantial reduction in CPU time. The results presented in this study may enable the simplification of complex arterial networks to increase the feasibility of meaningful full-body simulations in real-time.

2 Numerical Methodology

2.1 Geometry

The actual geometry of a descending aorta considered here is from patient-specific CT scan data obtained from the LPS Institute of Cardiology, Kanpur, India. The patient studied is a 40-year-old female and is otherwise anonymous. The reconstruction of the descending aorta is performed by the open-source software SimVascular v-2017 [26], in which the pathline of the center of the artery is traced, followed by segmentation of the peripheral region of the artery and surface generation. The selected artery length and details of the cross-sectional areas are given in Table 1. For the present study, the descending aorta is simplified into three levels. Level 1 is the original patient-specific artery created by the DICOM images arising from a CT scan. For the second level (simplified relative to the original, which we denote as Level 2), the original artery, i.e., Level 1, is divided into 25 slices, and a smooth CAD geometry is constructed based on the average diameter of the slices and is shown in Fig 1.

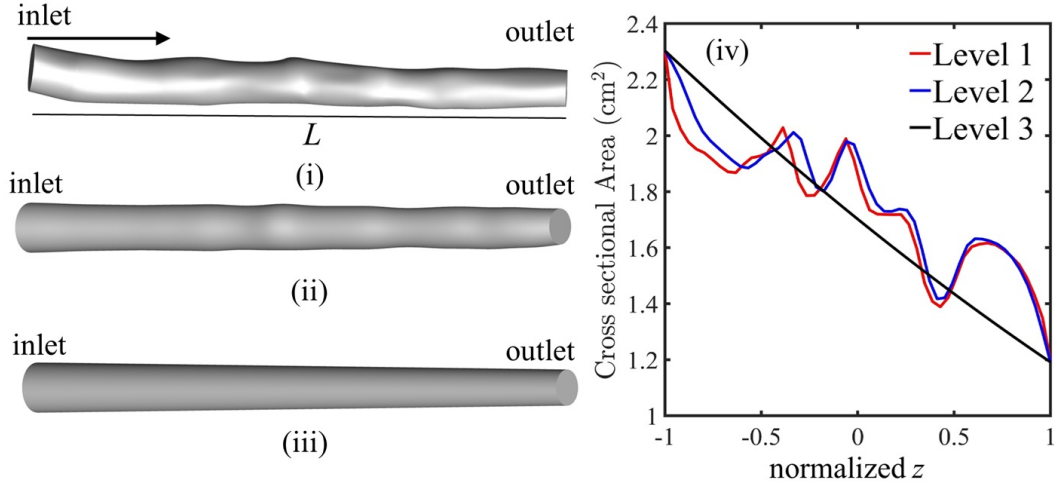


Figure 1: Level of geometrical aspects is shown, in (i) Level 1 of descending aorta extracted from CT-scan data, (ii) Slice-based geometry of descending aorta (Level 1 is divided into 25 slices for the construction of level 2). (iii) Level 3 geometry based on the inlet and outlet diameter of Level 1 geometry. (iv) Cross-section area variation over the normalized z -axis for each level of simplification of the descending aorta.

Level 2 is a simplified geometry that contains features of the original but is much coarser with fewer details. Next, we consider a highly simplified version that is a tapered smooth tube based on the inlet and outlet diameter, which we denote as Level 3. The three levels considered here represent a hierarchical simplification of the original geometry, retaining partial features of the original. It can be hypothesized that the grid requirements (and thus computational complexity) will be lower in smoother versions, but the loss of accuracy with regard to biomedical predictions remains to be investigated.

Table 1: Geometrical details of the realistic artery (Level 1) considered in the study

Dimensions	Symbol	Value
Artery length	L	17.2 cm
Inlet cross-section area	A_{in}	2.3 cm ²
Outlet cross-section area	A_{out}	1.2 cm ²

2.2 Governing equations

Patient-specific and simplified models of the arteries are used to study the hemodynamics of blood flow under pulsatile flow conditions. In this respect, the incompressible and unsteady form of the continuity and momentum equations are solved in three dimensions with realistic boundary conditions with appropriate viscosity models. The incompressibility constraint in the form of the continuity equation and the applicable momentum equations for a variable viscosity fluid are given below.

$$\nabla \cdot \mathbf{u} = 0 \quad (1)$$

$$\rho \left(\frac{\partial \mathbf{u}}{\partial t} + \mathbf{u} \cdot \nabla \mathbf{u} \right) = -\nabla p + \nabla \cdot \bar{\bar{\tau}} \quad (2)$$

Here \mathbf{u} is the velocity vector, p is pressure, and $\bar{\bar{\tau}}$ is the deviatoric part of the total stress tensor. The stress tensor is a function of the strain rate given as $\bar{\bar{\tau}} = \mu(\dot{\gamma})\bar{\bar{\gamma}}$, where $\bar{\bar{\gamma}} = \frac{1}{2}(\nabla \mathbf{u} + \nabla \mathbf{u}^T)$. The magnitude of the strain rate is given as $\dot{\gamma} = \sqrt{2\bar{\bar{\gamma}} : \bar{\bar{\gamma}}}$. Here μ is the apparent viscosity of blood based on the selected viscosity model.

2.2.1 Boundary Conditions

To solve the governing equations in the descending aorta and its simplified geometric versions, the following boundary conditions are applied:

1. Inlet conditions: A uniform velocity profile is imposed at the inlets of all geometries, combined with a pulsatile waveform to replicate the periodic nature of blood flow under physiological conditions. This pulsatile waveform captures the unsteady characteristics of flow and ensures a realistic simulation of the hemodynamic environment. The pulsatile velocity profile is derived from physiological measurements reported by Mills et al. [27]. The derived profile is fitted by a Fourier series of up to 18 terms to apply the inlet boundary condition with a mean $Re = 313$ and peak $Re = 1687$. To fully allow the inflow to develop into a Womersley profile, the inlet region of the artery is extended by a length of $10D$, where D represents the characteristic diameter of the artery. This extension minimizes upstream

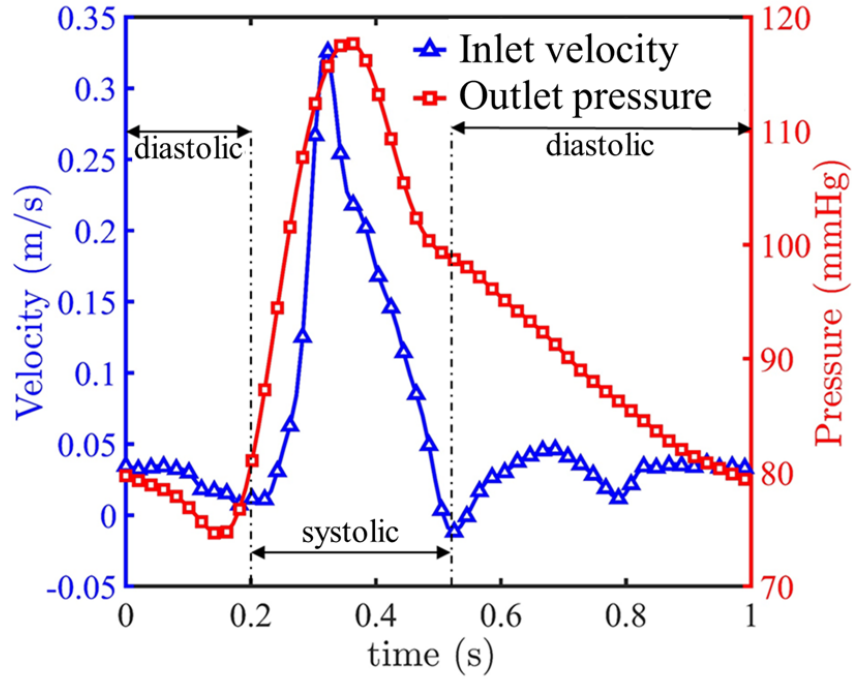


Figure 2: Pulsatile velocity waveform incorporated at the inlet of the artery along with the pulsatile pressure waveform at the outlet of the descending aorta. [27] .

flow irregularities owing to flow development and ensures a realistic inflow condition in the computational domain of interest. Similarly, an extension of $5D$ is added to the outlet to mitigate numerical reflections of an outflow boundary condition and maintain a smooth flow transition at the exit plane.

2. Outlet conditions: Realistic pulsatile gauge pressure is applied at the outlets of the geometries, as depicted in Figure 2. This boundary condition mirrors the dynamic pressure variation observed in the cardiovascular system, which are critical for accurately capturing the pressure-driven nature of blood flow. The pulsatile pressure profile is derived from physiological measurements carried out by Mills et al. [27], ensuring that they impose real-world conditions. These outlet conditions play a key role in maintaining the accuracy of flow characteristics, especially in scenarios where downstream vascular resistance and compliance significantly affect the upstream hemodynamics.
3. Wall conditions: The arterial walls in all geometries are assumed to be rigid, i.e. they do not deform under the influence of pressure and shear

loading. A no-slip boundary condition is enforced at the walls, requiring the velocity at the wall to be zero. This assumption is widely used in computational blood flow simulations. Since a rigid wall is expected to display the strongest vortical structures.

2.2.2 Blood viscosity models

The selection of the viscosity model is essential to simulate realistic blood flow characteristics. Blood is a non-Newtonian fluid, but since shear rates are smaller in vessels of large diameters, non-Newtonian effects are less pronounced here. For such arteries, earlier studies have shown only minor differences in predictions from Newtonian and non-Newtonian models in tubular geometries. For the geometry considered in the present study, surface perturbations are present in Level 1 and differences in predictions across models may be expected. Thus, in this study, we consider the Newtonian and two non-Newtonian models for blood viscosity. The selected viscosity models are discussed below.

1. Newtonian

The Newtonian model [28] is widely employed in blood flow simulations, primarily due to its linearity and the resulting computational efficiency. It is expected that for arteries of relatively larger size, Newtonian model predictions are negligibly different from the non-Newtonian ones. In the present study, blood viscosity is taken to be a constant, namely

$$\mu_{app} = 0.0035 \text{ Pa s} \quad (3)$$

It is appropriate for a body temperature of 310 K.

2. Carreau-Yasuda

The Carreau-Yasuda [29] is one of the most widely used Generalized Newtonian fluid (GNF) model. For viscoelastic fluids, the Carreau-Yasuda model is more realistic than the Power-law model since it shows a plateau at both low and high shear rates. Specifically, blood demonstrates near-constant viscosity at high shear rates, consistent with the assumptions of a Newtonian fluid under such conditions. The Carreau-Yasuda viscosity

model is given as:

$$\mu_{app} = \mu_0 + (\mu_0 - \mu_\infty)(1 + (\lambda\dot{\gamma})^P)^{\frac{n-1}{P}} \quad (4)$$

In this context, μ_0 and μ_∞ are the saturation values of viscosity at low and high shear rates, respectively. The parameter P is known as the Yasuda exponent, with both P and n determining the degree of nonlinearity. The time constant λ regulates the range of strain rates at which the transition to a power-law type regime is obtained. In this way, λ is related to the relaxation time of the fluid. The model simplifies to the Newtonian fluid when the time constant is zero ($\lambda = 0$). Table 2 lists the parameters used for the Carreau-Yasuda model for blood in this study.

Table 2: Parameters considered for the Carreau-Yasuda blood viscosity model at a body temperature of 310 K

Carreau-Yasuda Viscosity Parameters	Value
μ_0	0.056 Pa·s
μ_∞	0.0035 Pa·s
λ	3.313 s
n	0.3568
P	2

3. Apostolides and Beris

The recently developed viscosity model by Apostolides and Beris [30] is based on the Casson viscosity model. The parameters are functions of the constituents of blood such as hematocrit concentration ϕ and fibrinogen c_f , whose values are adjusted using various flow-related data available in the literature. The apparent fluid viscosity is given by the following equation:

$$\mu_{app} = \left(\sqrt{\frac{\tau_0}{\dot{\gamma}}} + \sqrt{\mu_c} \right)^2 \quad (5)$$

Here, $\dot{\gamma}$ is the magnitude of the strain rate while the yield stress τ_0 is given as follows:

$$\tau_0 = \begin{cases} (\phi - \phi_c)^2 [0.508c_f + 0.4517]^2, & \text{if } \phi > \phi_c; \\ 0, & \text{if } \phi \leq \phi_c; \end{cases} \quad (6)$$

A threshold value of hematocrit is required to calculate the yield stress; this threshold is a quadratic function of the fibrinogen concentration.

$$\phi_c = \begin{cases} 0.312c_f^2 - 0.468c_f + 0.1764, & c_f < 0.75; \\ 0.0012; & c_f \geq 0.75; \end{cases} \quad (7)$$

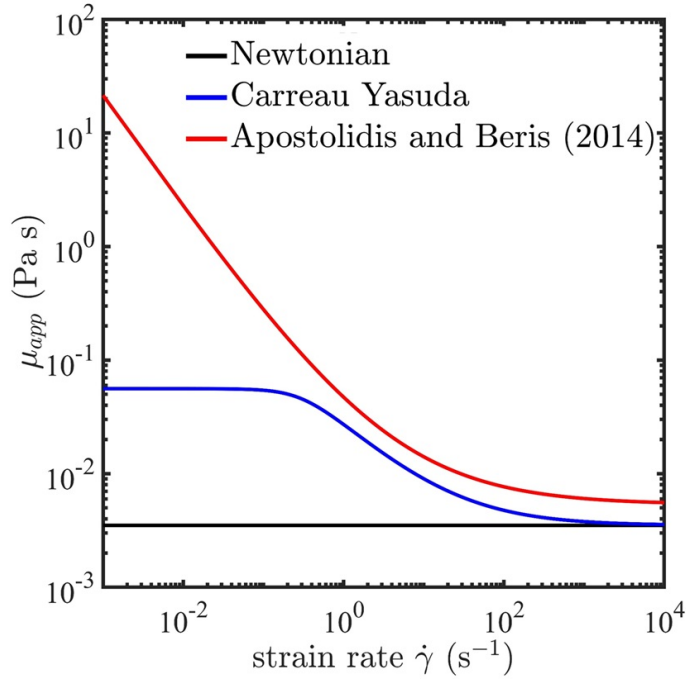


Figure 3: Blood viscosity models selected for simulating the blood flow in the descending aorta. Newtonian, Carreau Yasuda, and Apostolidis and Beris models are shown.

The Casson viscosity, i.e., μ_c , is also obtained by using the experimental data available in the literature and follows an Arrhenius dependence on temperature, given as:

$$\mu_c = \mu_p(1 + 2.0703\phi + 3.722\phi^2) \exp \left[-7.0276 \left(1 - \frac{T_0}{T} \right) \right] \quad (8)$$

At fully developed conditions, the local shear rate is zero at the center of a smooth circular channel. This local shear rate will make the apparent viscosity infinitely large, leading to an instability in the numerical solver. To ensure the stability of the solver at fully developed conditions, Miller

and Morris [31] suggested that the shear rate magnitude is regularised as $\dot{\gamma} = \dot{\gamma} + \dot{\gamma}_r$, where the non-local shear rate $\dot{\gamma}_r \ll \dot{\gamma}$ and given as

$$\dot{\gamma}_r = \frac{\epsilon U_{max}}{L_c}$$

Here, U_{max} is the maximum velocity attained in the Newtonian viscosity model, $\epsilon = 0.01$ is the regularization parameter, and L_c is the characteristic length. In the present study, it is chosen as the inlet diameter of the Level 1 artery. The parameters selected are appropriate for a normal human body temperature of 310 K and summarized in Table 3.

Table 3: Parameters considered for the Apostolidis and Beris blood viscosity model [30]

Blood Parameters for the Apostolidis and Beris Viscosity Model	Value
Average hematocrit concentration, ϕ	0.4
Temperature of Blood Sample, T	310 K
Reference Temperature, T_0	296.1 K
Plasma viscosity, μ_c	1.67×10^{-3} N·s/m ²
Density of blood, ρ	1060 kg/m ³
Fibrinogen concentration, c_f	0.125 g/dl

3 Flow distribution in a descending aorta

3.1 Grid Independence Test and Validation

3D simulations of the flow distribution in the descending aorta in patient-specific (Level 1) and its simplified versions (Levels 2 and 3) are performed using the finite volume method within ANSYS-Fluent®, a commercial flow solver. For the grid independence test for the three geometries, the steady flow problem is solved on four refined meshes (M1, M2, M3, and M4). The solver used in this study is also validated with the results of Nagargoje et al. [32] for a symmetric bifurcation with pulsatile inlet boundary conditions. The pulsatile waveform and the geometry of interest are shown in Figure 4. In Figure 5(a), the average velocity obtained is shown as a function of the inverse of the mesh element size. Following grid independence, the M3 mesh is selected for further

simulations. Validation against the work of [32] is shown in Figure 5(b). The z -component velocity is plotted on the centerline near the bifurcation for three-time instants of the oscillatory inflow condition. The validation results are seen to be satisfactory, which provides a check on the correctness of the solver.

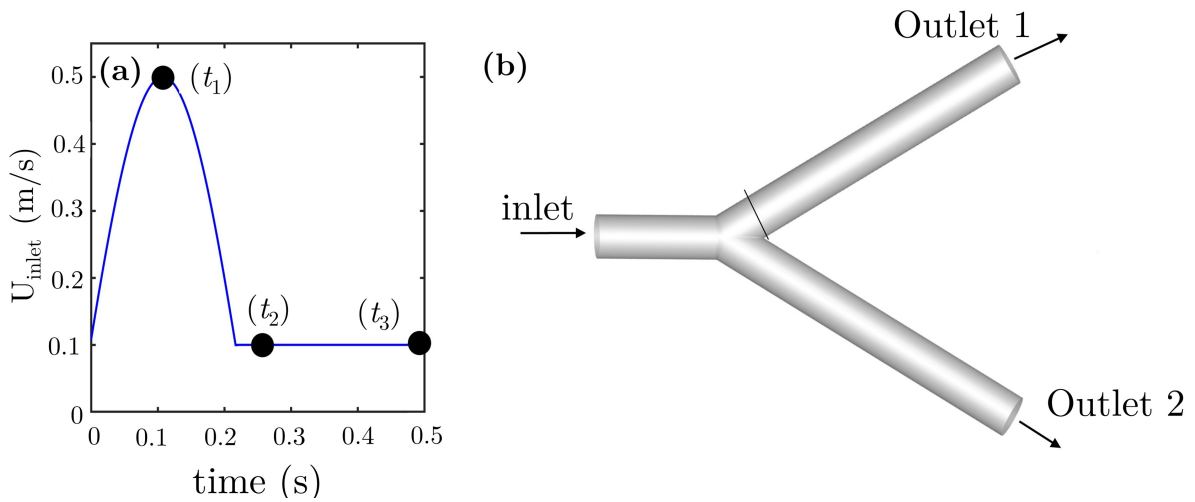


Figure 4: (a) Oscillatory velocity inlet profile. (b) symmetric bifurcation geometry used by Nagargoje et al. [32]

Next, flow metrics and hemodynamic parameters are analyzed to understand the implications of the geometric simplifications for the three viscosity models. Quantities of interest are the velocity profiles and wall shear stress, along with the hemodynamic parameters such as the time-averaged wall shear stress (TAWSS) and Oscillatory Shear Index (OSI). Analysis in terms of the Q-criterion for strain rate and rotation are also reported.

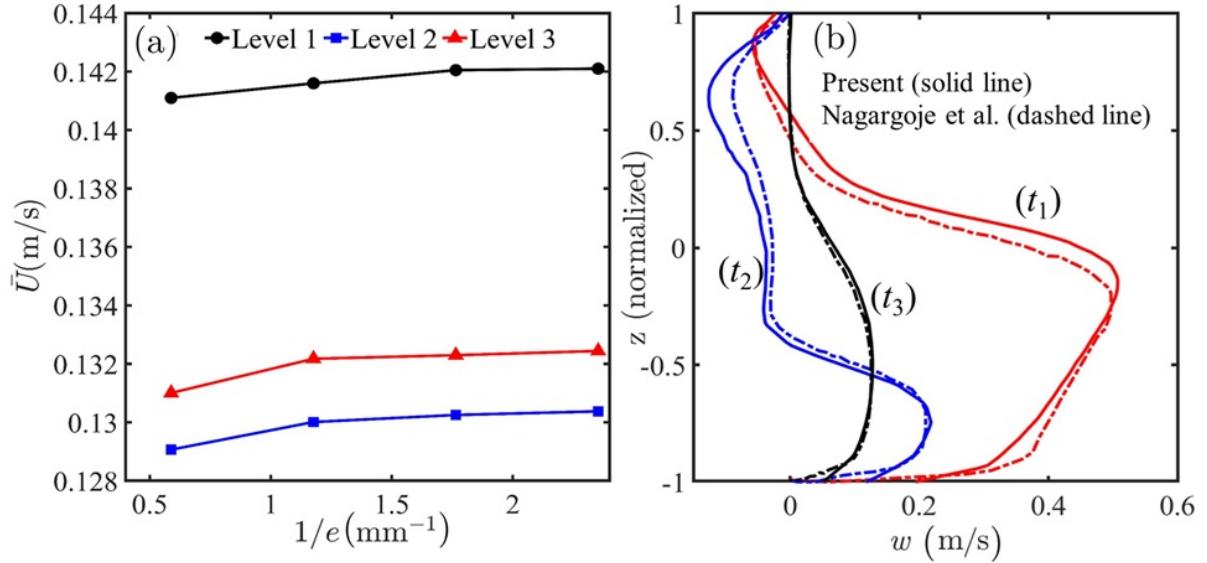


Figure 5: (a) Mesh independence test is performed for Levels 1-3 of the descending aorta. The average velocity at the outlet is presented as a function of the inverse of the mesh element size. Here, e is the mesh element size, and a higher inverse element size indicates a finer mesh. (b) The z -velocity component (w) is plotted at time instants t_1 , t_2 , and t_3 at the bifurcation of the geometry and matched against comparable results of Nagargoje et al. [32]

3.2 Velocity Profiles

This section presents the cross-sectional velocity distribution during the systolic and diastolic phases over various planes of the descending aorta for the three viscosity models and Levels 1-3 geometries. The velocity data are shown in Figures 6 and 7 for the 4th cycle of simulation since the flow was shown to exhibit clear periodicity after the third cycle, indicating a fully developed dynamic steady state. Specific time instants from the cycle, as highlighted in left-most columns of Figures 6 and 7 are used for discussion.

The systolic phase of the waveform (Figure 2) includes three key instants: $t_1 = 0.2$ s in the initial instant of increase in inflow velocity, $t_2 = 0.3$ s is the peak, and $t_3 = 0.45$ s is the deceleration phase. The diastolic phase is analyzed at two time instants, $t_4 = 0.6$ s and $t_5 = 0.7$ s, representing flow fluctuation towards the end of the cycle. This section further describes the velocity characteristics over the cross-section in the form of centerline plots along with streamlines, contours, and vectors for the selected viscosity models and geometric simplification levels.

In Figures 6 and 7, the distribution of the axial velocity component (denoted by u) is shown at the centerline of the cross-section located at a distance of $z = 16D$ from the extended inlet as a function of the normalized y -coordinate. We show a comparison across two factors; in the first set of figures (Figure 6), we focus on comparing the viscosity models for a particular level of simplification, which shows subtleties in model predictions. In Figure 7, we show a comparison across the level of simplification for any given viscosity model. This completes the picture and shows how modeling aspects are coupled with geometry details. In Figure 6, each level of geometry simplification is shown in a column, while rows represent distinct phases of the pulsatile flow cycle. The velocity profiles, normalized across the channel width, are depicted by red, blue, and black lines for the Newtonian, Carreau-Yasuda, and Apostolidis-Beris models, respectively. The axial velocity component distribution is shown at the selected time instants for the individual viscosity models for a particular geometry simplification level. An asymmetric velocity distribution is observed for Level 1 only. This is expected since the perturbation and undulations across the circumference at any axial position are retained in Level 1, which leads to an asymmetric flow in succeeding cross-sections. Interestingly, in Level 1, the flow profiles are nearly identical for all phases of the cycle for the Newtonian and Carreau-Yasuda viscosity models. This similarity is expected since the Newtonian and Carreau-Yasuda models predict similar viscosities at high shear rates (Figure 3). The velocity predictions for the Apostolidis and Beris viscosity model are slightly larger than the other two for all the phases. For Level 2 (Figure 6(b)), the geometry is simplified and made symmetric around the circumference, and symmetric flow profiles are observed for all the viscosity models at every phase of the pulsatile flow. Interestingly, at this level, the two non-Newtonian models - Carreau-Yasuda and Apostolidis and Beris- predict similar velocity profiles, whereas the Newtonian predictions show an overshoot near the centerline. Note that such differences at the centerline are known between Newtonian and non-Newtonian models for flows in a smooth duct where the latter needs a resolution of the shear rate singularity within the definition of apparent viscosity. For the simplest Level 3 in Figure 6(c) which is a tapered smooth tube, the predictions

across viscosity models are largely symmetric and similar to each other, owing to the symmetry of the geometry.

Next, in Figure 7, we show the velocity comparison across geometry simplifications for each viscosity model. The data shows an accuracy check for such simplifications across different viscosity models considered in the present study. Columns (a), (b), and (c) depict the velocity profiles for the Newtonian, Carreau-Yasuda, and Apostolidis and Beris viscosity models, respectively. As mentioned earlier, the rows represent distinct phases of the pulsatile flow cycle. Largely, the trends agree with each other, except for the asymmetry that is only visible for the patient-specific geometry (Level 1). The largest differences are observed at the start of the cycle (first row) and during the deceleration phase (third row). Interestingly, for the deceleration phase, only the predictions with the combination of Level 3 and Newtonian fluid are significantly more than the others. Thus, with respect to velocity profiles, the simplified geometry can capture the trends quite well for all viscosity models, except for the expected asymmetry in Level 1.

In what follows, further analyses in terms of streamlines, velocity contours, and vectors are provided. Figure 8a shows velocity magnitude contours at various cross-sectional planes in the descending aorta in the Level 1 geometry for various phases of the inflow waveform. Additionally, Figure 8b displays the velocity magnitude combined with streamline plots over the medial plane of the Level 1 aorta. These details are presented here for the Apostolidis and Beris viscosity model. The key trends remain similar to the other two models and hence, are not repeated. During the systolic phase, the inflow increases steadily, reaching a peak corresponding to the maximum flow rate. This progressive increase in inflow elevates wall forces, consequently enhancing wall loading. In contrast, the diastolic phase exhibits a much more complex flow behavior, driven by the adverse pressure gradient that develops as the inflow decelerates in time. The adverse gradient generates regions of backflow where the flow reverses direction near the walls.

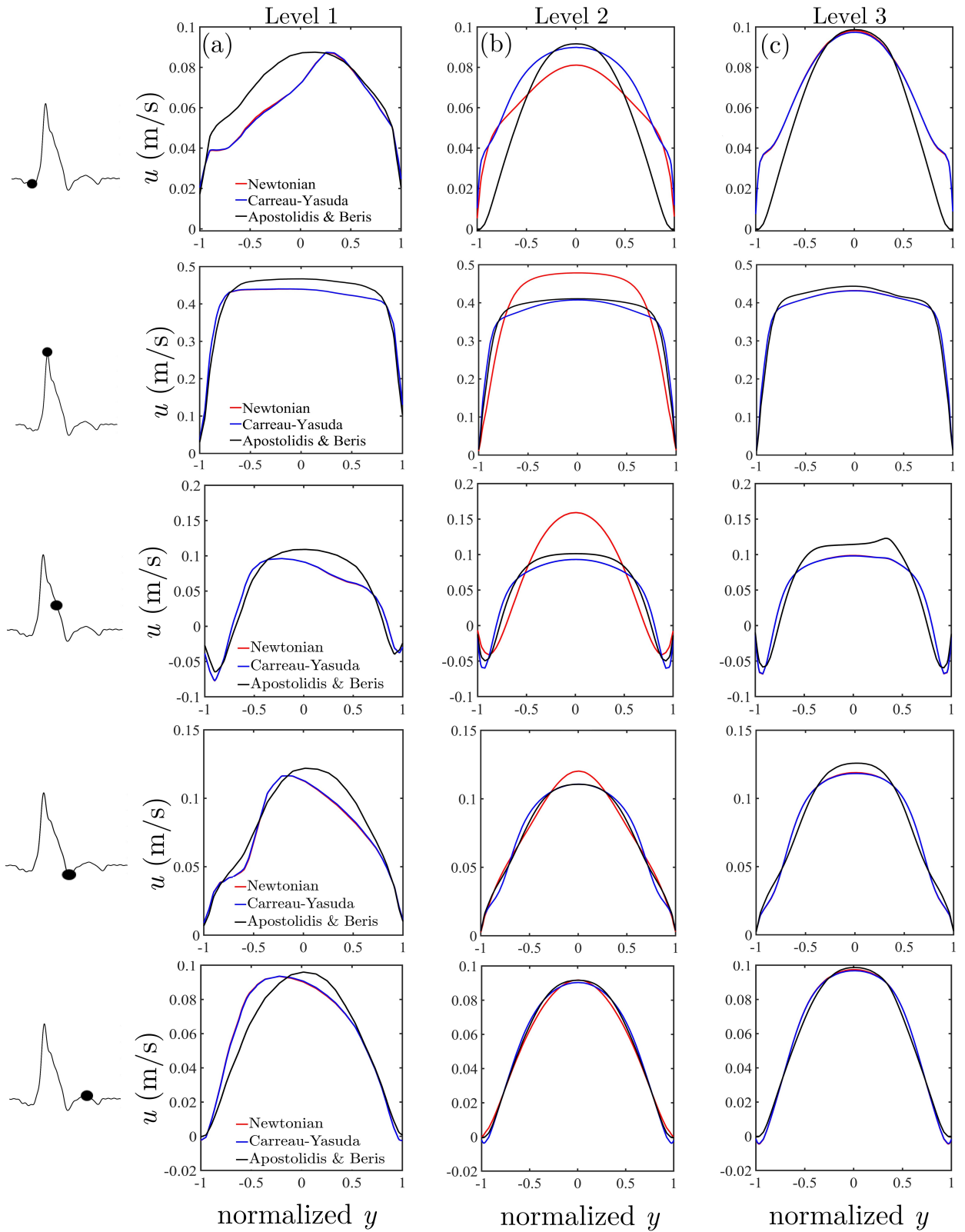


Figure 6: Axial velocity component shown for the three different viscosity models in (a) Level 1, (b) Level 2, and (c) Level 3 geometries.

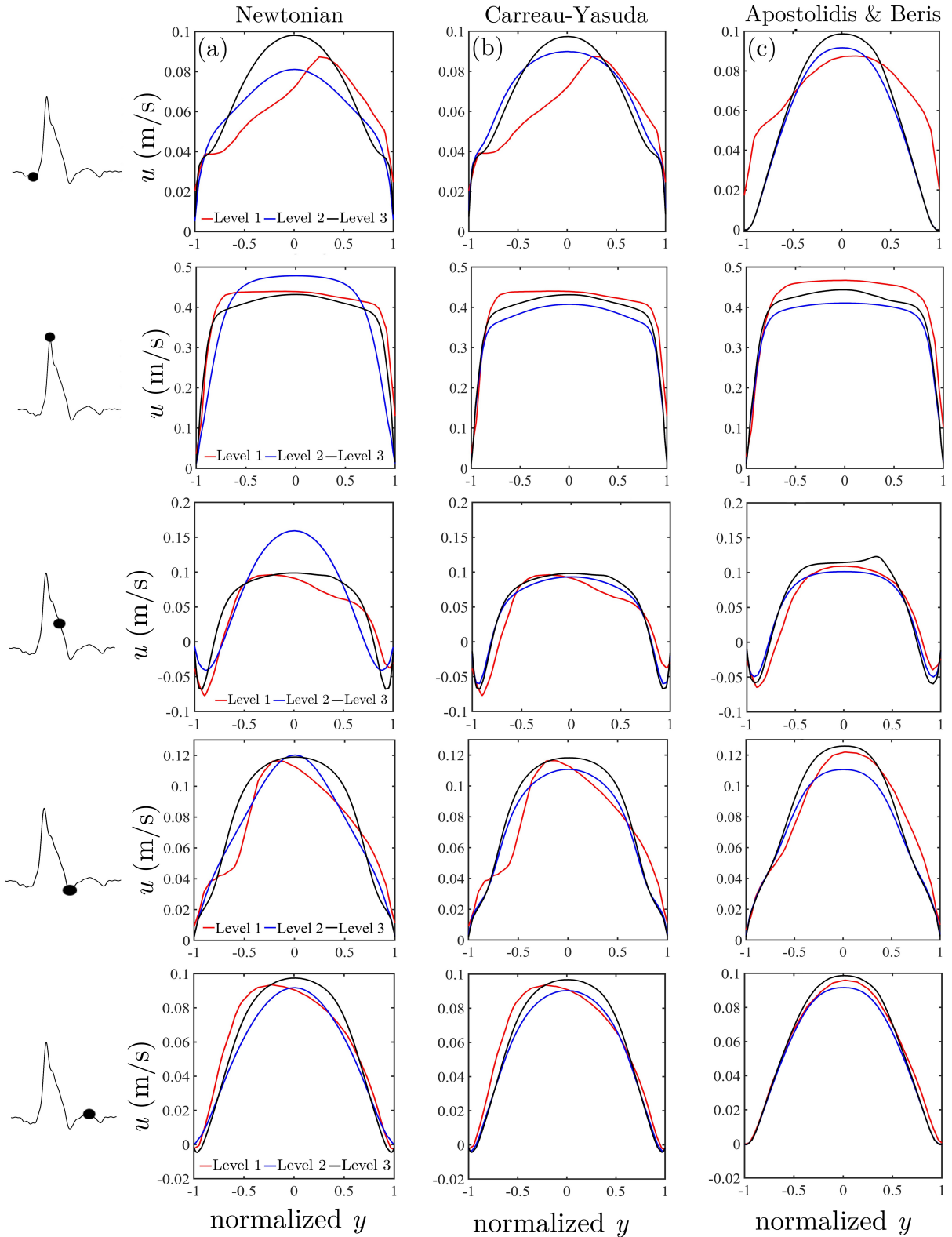


Figure 7: Axial velocity component shown for the original and two simplified geometries (Levels 1-3) for (a) Newtonian, (b) Carreau-Yasuda, and (c) Apostolidis and Beris viscosity models.

These regions are particularly pronounced in areas with irregular geometry

or abrupt changes in cross-section and surface perturbations. The backflow generated disrupts the unidirectional flow and interacts with the surrounding fluid, leading to flow separation and the formation of recirculation zones. The interplay between backflow, flow circulation, and pressure gradients indicates the sensitivity of the flow field to boundary conditions and geometric variations and reinforces the importance of retaining details in the geometry. Thus, a prediction accuracy loss is expected with geometry simplifications, some of which are examined next in Figure 9.

Streamlines in the three geometries at all time instants are shown in Figure 9 with the Apostolidis and Beris viscosity model. It is observed that during the systolic phase, all the streamlines are unidirectional and no flow circulation is observed. However, as the flow enters the diastolic regime, flow circulations appear in Level 1 as well as Level 2 but are completely absent in Level 3. These flow recirculation zones are a result of the interplay of the geometrical perturbations and adverse pressure gradient conditions. With the absence of perturbations in Level 3, such zones of backflow are absent. Reversed flow zones are also larger in Level 1, relative to Level 2, owing to geometric variations coupled with a loss of symmetry. Thus, as the artery geometry is simplified, the intensity of circulation decreases and disappears in the limit of the smooth geometry approximation, namely, Level 3. Flow circulation patterns are important from a medical point of view since they affect the wall shear stress (WSS) and pressure loading. The circulation region being stagnant will promote particulate deposition leading to thrombosis. Hence, delineating such regions is important from a biomedical perspective.

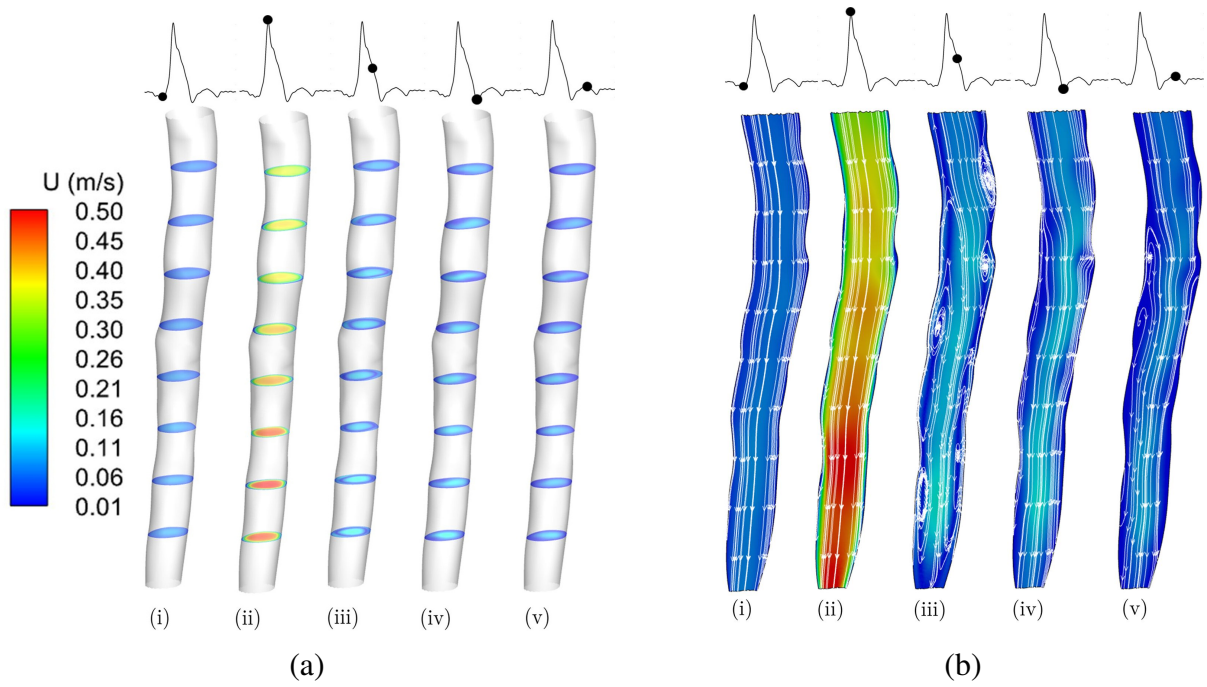


Figure 8: (a) Velocity magnitude contours at various time instants for Level 1 artery and (b) streamlines superimposed on the velocity magnitude contour over the median plane for the Apostolidis and Beris viscosity model. (i)-(iv) show distinct phases of the vascular waveform.

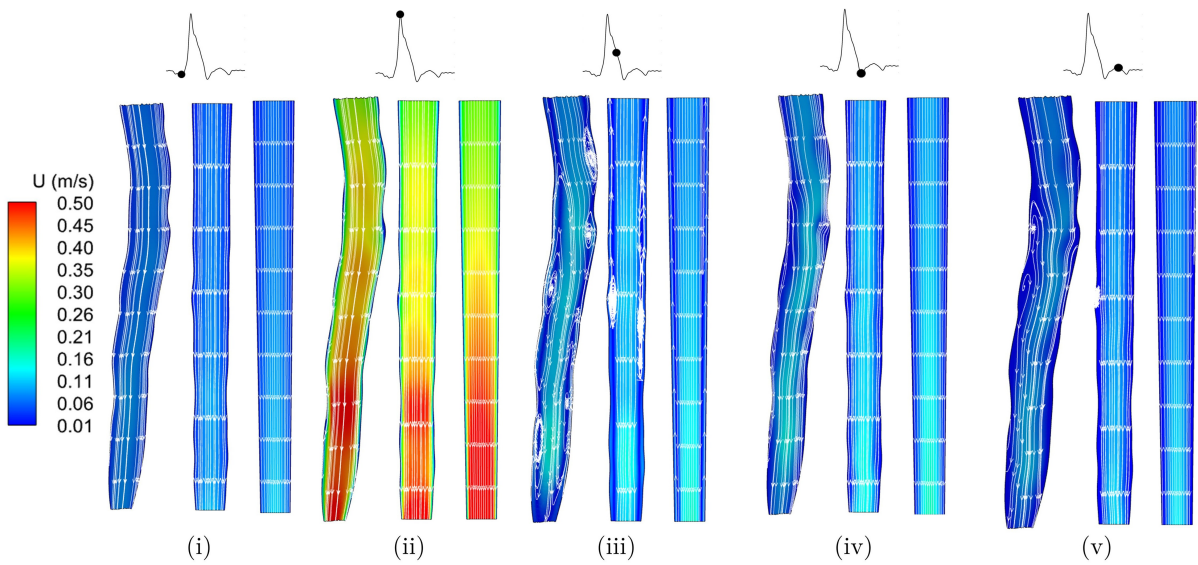


Figure 9: Velocity contours superimposed with streamlines are shown at selected time instants for the Apostolidis and Beris viscosity model for the three geometry levels 1-3. Within (i)-(v), Levels 1 to 3 are shown from left to right.

3.3 Hemodynamic Parameters

3.3.1 Wall shear stress (WSS)

Wall shear stress (WSS) plays a crucial role in regulating the endothelial function and has been widely recognized as a key factor in the development of atherosclerosis. Endothelial cells sense the wall shear stress via multiple responsive cell components, and activation or deactivation of intra-cellular pathways leads to gene and protein expression regulation [33]. This continuous process is important for remodeling, development, and growth of the vascular walls. Moreover, clinical significance of wall shear stress lies in its ability to predict the risk of future cardiovascular events, making it an important biomarker in cardiovascular health. Mathematically, WSS can be calculated with the help of velocity gradients ($\nabla \mathbf{u}$) as follows:

$$\bar{\tau}_w = 2\mu_{app}\bar{\dot{\gamma}} \quad (9)$$

The strain rate ($\bar{\dot{\gamma}}$) is given by the sum of the velocity gradient and the transpose of the velocity gradient $\frac{1}{2}(\nabla \mathbf{u} + \nabla \mathbf{u}^T)$ at the wall. The magnitude of the strain rate tensor field can be calculated as $\dot{\gamma} = \sqrt{2\bar{\dot{\gamma}} : \bar{\dot{\gamma}}}$. Wall shear stress is calculated for the patient-specific and simplified geometries (all levels) and presented in the form of contours. The wall shear stress (WSS) contours are shown in Figure 10 for all the time instants of the pulsatile cycle for the original and other geometric simplification levels while adopting the Apostolidis and Beris viscosity model. The features of WSS in Level 1 are particularly significant in predicting the onset and progression of disease, as they provide detailed insights, as well as the identification of the critical regions.

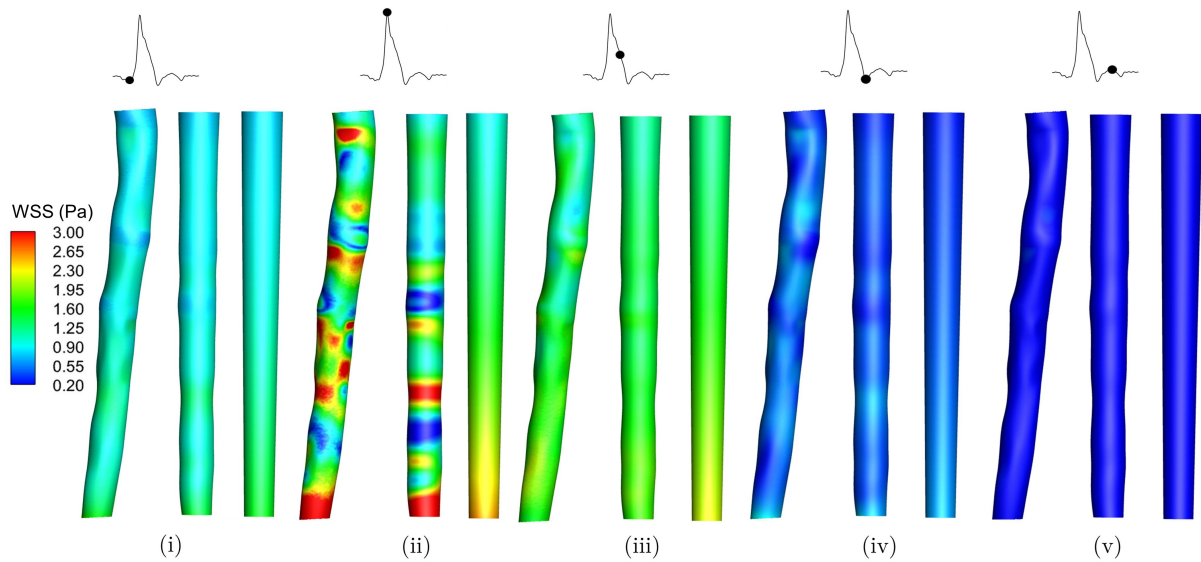


Figure 10: Wall shear stress (WSS) contours superimposed with streamlines are shown at the selected time instants of the vascular cycle for the Apostolidis and Beris viscosity model. Within (i) to (v), Levels 1 to Level 3 are shown from the left.

Figure 10 shows how the simulation accuracy deteriorates by simplifying the geometry. Firstly, for Level 1, with all perturbations preserved, we observe high variability in WSS at the peak instant of flow. At all times, the surface perturbations and the asymmetry generate several high (and low) stress zones of WSS. Some of these variabilities are captured in Level 2, although the asymmetry of Level 1 is lost. The high and low-stress zones appear as bands around the circumference, with an overall reduction of the variations observed in the WSS distributions of Level 1. This is most pronounced at the time instant of peak velocity. However, the WSS profile is smooth at Level 3 (tube of decreasing area), and all the variability is lost. Thus, Level 2 might still provide satisfactory predictions of WSS, which is entirely lost in Level 3. The variability in these hemodynamic parameters, in terms of the maximum and minimum values, are shown in Table 4 in a tabular form. For simplicity, for all three viscosity models, we show the data only at two time instants of the cycle - $t = 0$ s and $t = 0.35$ s (peak). The table further highlights the discussion about the accuracy of Levels 2 and 3 (relative to level 1) presented above. The table further shows that while the values in Level 2 retain some similarity, the values for Level 3 are significantly different in most cases. These trends broadly fit the

discussion presented above.

Table 4: Minimum and maximum wall shear stress magnitude values recorded at the start ($t = 0$ s) and at the peak ($t = 0.35$ s) of the cardiac cycle for the simplified geometrical levels and tabulated for the selected viscosity models.

time	Geometry →	Level 1		Level 2		Level 3	
	Viscosity models ↓	min	max	min	max	min	max
$t = 0$ s	Apostolidis & Beris	0.170	0.647	0.209	0.686	0.230	0.527
	Carreau-Yasuda	0.014	0.398	0.037	0.371	0.067	0.229
	Newtonian	0.011	0.401	0.394	1.385	0.062	0.223
$t = 0.35$ s	Apostolidis & Beris	0.029	5.930	0.004	3.960	0.378	1.444
	Carreau-Yasuda	0.006	2.642	0.000	2.807	0.100	0.764
	Newtonian	0.004	2.642	0.001	2.949	0.094	0.756

3.3.2 Correlations

The previous discussion on retention of accuracy is qualitative. To enable the quantification of the impact of simplified geometric levels on accuracy, we introduce a correlation metric here. These correlations can be used to compare the accuracy levels of any hemodynamic parameter across the descending aorta. Here, we show the definition of the correlation for the WSS, but it can also be extended to pressure. The calculations use the deviations of any parameter from its mean at any location, as follows:

$$\theta = \text{WSS}_c - \overline{\text{WSS}_c}; \text{ for wall shear stress.} \quad (10)$$

Here, $\overline{\text{WSS}_c}$ is the average over the length of the artery, circumferential average wall shear stress (WSS_c) at any location and θ is the deviation parameter. The deviation parameter θ is calculated for the simplified levels of the descending aorta, i.e., θ_1, θ_2 and θ_3 for Level 1, Level 2 and Level 3, respectively. Keeping Level 1 as a reference, the correlation (C) between the different geometry levels is defined as:

$$C_{11} = \frac{\sum_z \theta_1 \theta_1}{\sum_z \theta_1 \theta_1} = 1; C_{12} = \frac{\sum_z \theta_1 \theta_2}{\sum_z \theta_1 \theta_1}; C_{13} = \frac{\sum_z \theta_1 \theta_3}{\sum_z \theta_1 \theta_1}; C_{23} = \frac{\sum_z \theta_2 \theta_3}{\sum_z \theta_2 \theta_2}; \quad (11)$$

where C_{12} , C_{13} and C_{23} are the correlation parameter between levels 1 and 2, levels 1 and 3 and levels 2 and 3, respectively. By definition, C_{11} should be unity and is used in the plots for validation. Thus, correlation parameters provide a sense of a “hotspot” (in WSS or pressure) being observed at a similar location when two different geometry levels are used. If a simplified geometry is able to capture all hotspots of level 1 at their respective locations, the value of the correlation parameter would be close to unity.

Here, we evaluate correlation levels for WSS and pressure. These correlations are computed at specific time instants of the waveform. The correlation coefficient, C , is evaluated for the wall shear stress (WSS) magnitude and wall pressure over the entire cardiac cycle for the selected viscosity models, and the results are presented in Figure 11. The correlation trends for both WSS (Figure 11(a)) and wall pressure (Figure 11(b)) are examined. The WSS values of C_{12} remain close to unity for the non-Newtonian models but show large fluctuations for the Newtonian model. In contrast, C_{13} and C_{23} remain further away from unity. This quantitatively supports our preceding discussion. For WSS, Level 2 predictions remain highly correlated with Level 1 (and thus retain accuracy), whereas much of this accuracy is lost in Level 3. However, the Newtonian model is not well behaved for these simulations, showing large fluctuations in correlation values across models. Particularly, cross-correlations C_{12} and C_{13} are large during phases C and D for the Newtonian simulation, suggesting the role of the flow structures appearing in Level 1. This perhaps indicates that the non-Newtonian models of blood should be used for such simulations in geometries that contain a high degree of irregularity. Conversely, accuracy loss is observed to be mild in pressure values.

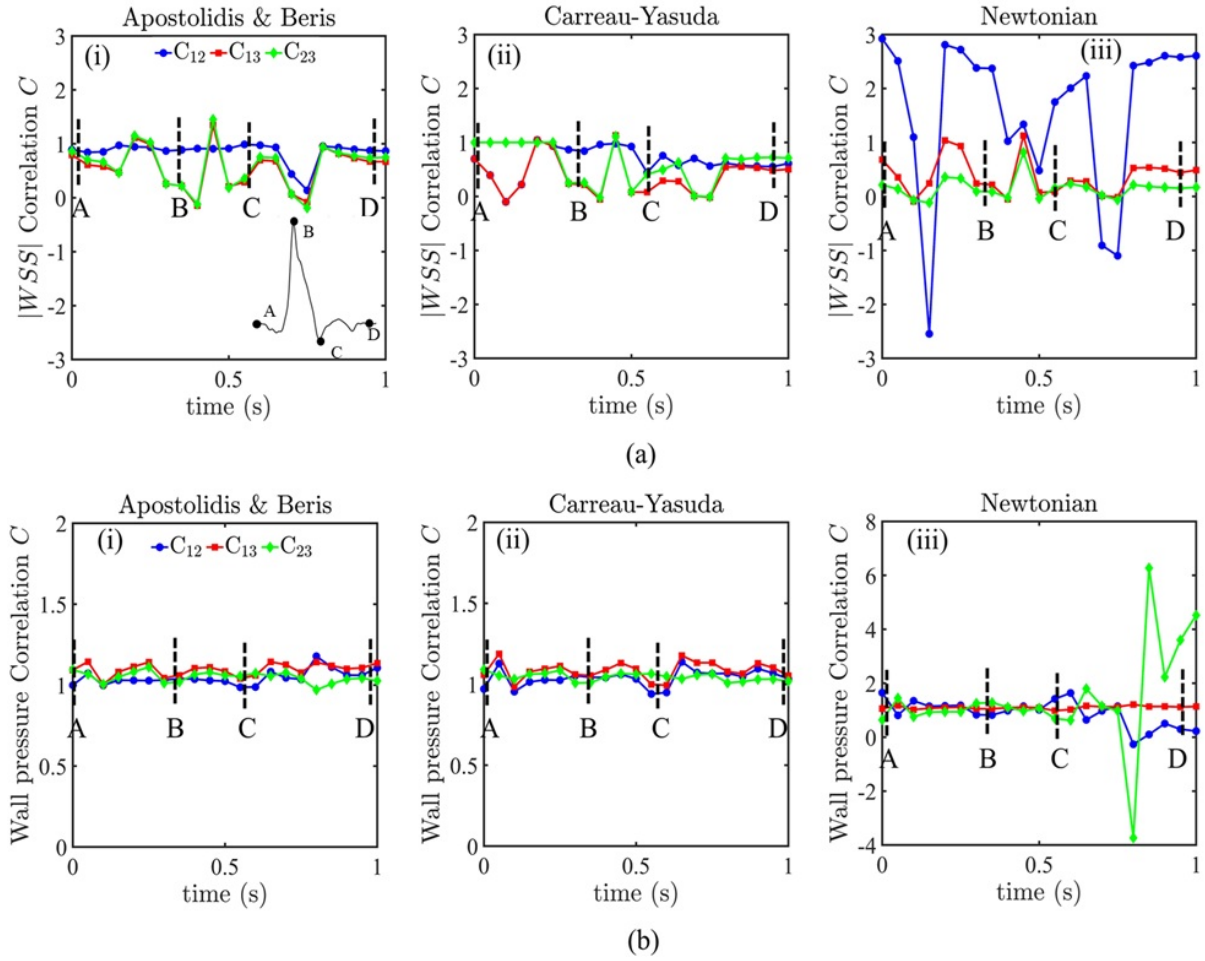


Figure 11: Correlations of (a) wall shear stress magnitude and (b) wall pressure are plotted with time for the selected viscosity model, i.e., (i) Apostilidis and Beris, (ii) Carreau-Yasuda and (iii) Newtonian. The correlation parameter values are highlighted at phases of the velocity waveform given at $t = 0$ s (A), $t = 0.35$ s (B), $t = 0.55$ s (C), and $t = 0.9$ s (D).

3.3.3 Time-averaged wall shear stress (TAWSS)

Along with WSS, time-averaged wall shear stress (TAWSS) is a primary risk parameter to monitor the development and progression of atherosclerosis, which can further lead to various types of cardiovascular diseases. Both low and high-wall shear stress promotes pro-inflammatory and anti-inflammatory responses by the endothelial cells [31]. An average WSS over the cardiac cycle is the time-averaged wall shear stress (TAWSS), which further helps identify the high and

low WSS zones. Mathematically, TAWSS is defined by the following relation:

$$\text{TAWSS} = \frac{1}{T} \int_0^T |\tau_w| dt \quad (12)$$

Here, T is the time period of the cardiac cycle. Time-averaged wall shear stress (TAWSS) calculated for the fourth cycle of the simulations is shown in Figure 12 for the three levels of the geometry of the descending aorta and selected viscosity models. In Figure 12 (i),(ii) and (iii) TAWSS contours are plotted for Apostolidis and Beris, Carreau Yasuda, and Newtonian viscosity models, respectively. The trends are qualitatively similar to WSS discussed earlier. In Level 1, the perturbations and asymmetry of the geometry generate a significant amount of zones for high and low TAWSS. Some of these zones are retained in Level 2 with less asymmetry and a reduction in the shear stress magnitudes. A gradual variation of TAWSS is obtained in Level 3 which is a smooth geometry. The trends are similar across the three viscosity models. However, the perturbations in TAWSS are slightly different with the Apostolidis and Beris model, whereas the profiles are similar for the Newtonian and Carreau-Yasuda models. The values are slightly higher with the Apostolidis and Beris model in Level 1. Thus, again, concerning spots of extreme stress, Level 2 captures the essence partially while variations in Level 3 are averaged out.

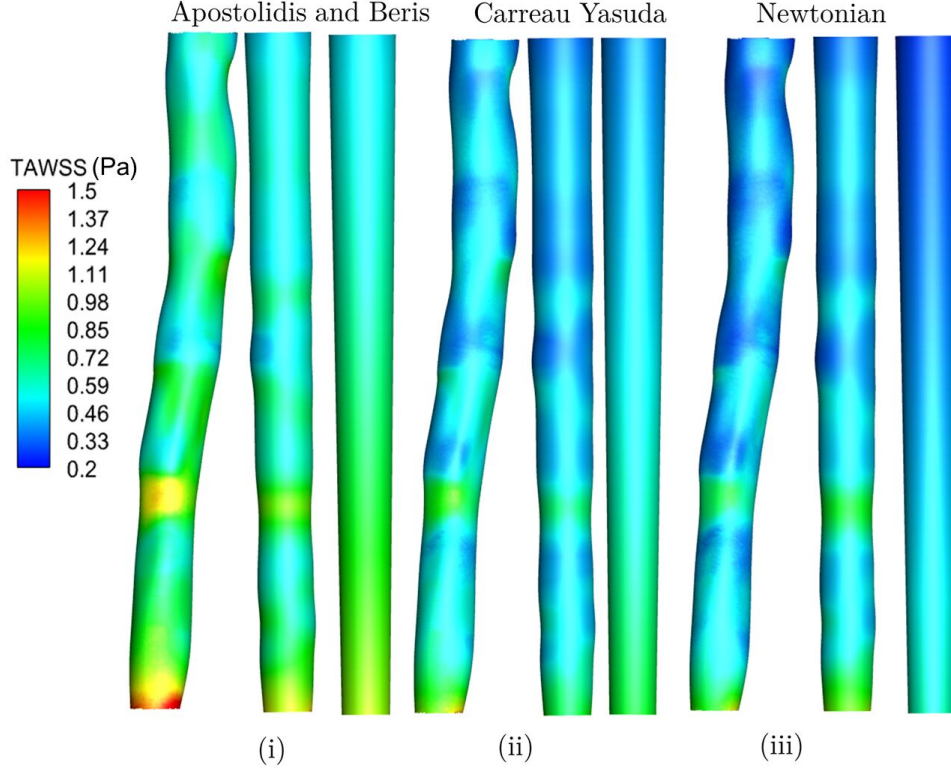


Figure 12: Time average wall shear stress (TAWSS) shown for the three viscosity models for Levels 1,2 and 3 geometry of the descending aorta. (a) Apostolidis and Beris, (b) Carreau-Yasuda and (c) Newtonian viscosity model.

3.3.4 Oscillatory shear index (OSI)

In pulsatile flow, the shear stress near the artery wall fluctuates, making the endothelial cell deliver a pro-inflammatory response. The Oscillatory Shear Index (OSI) introduced by Ku et al. [34] provides a measure of these fluctuations. The OSI can be calculated as follows:

$$\text{OSI} = \frac{1}{2} \left(1 - \frac{|\int_0^T \tau_w dt|}{\int_0^T |\tau_w| dt} \right) \quad (13)$$

OSI varies between 0 and 0.5, the latter representing a purely oscillatory response. The high-value region shows a high time-periodic oscillation of the wall shear stress.

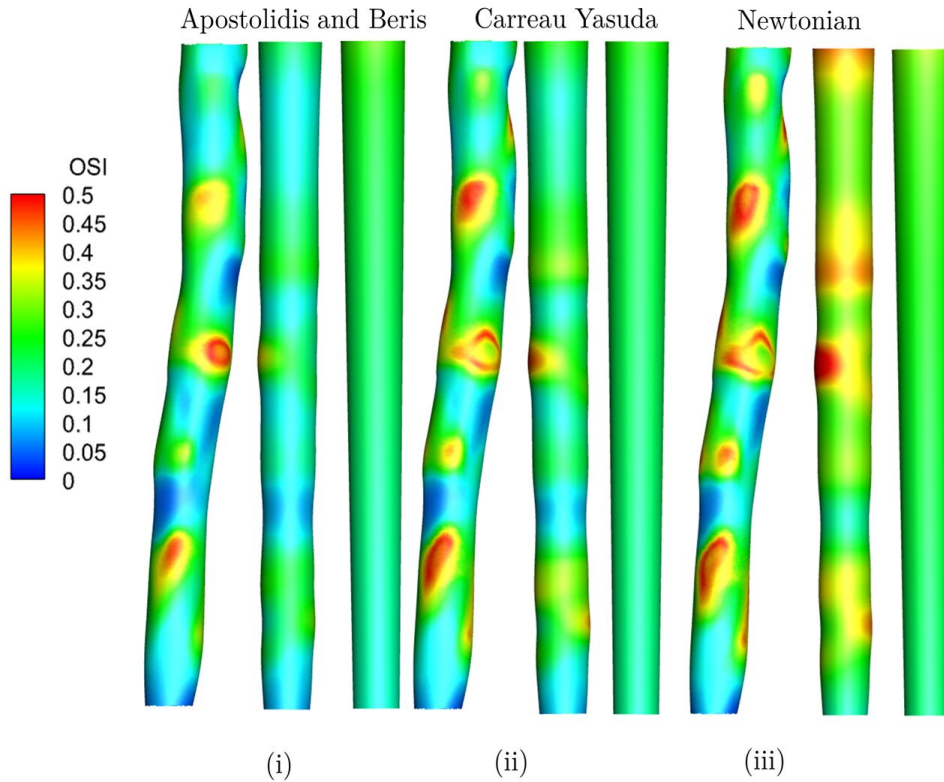


Figure 13: Oscillatory shear index (OSI) shown for the three viscosity models for Levels 1,2 and 3 geometry of the descending aorta. (a) Apostolidis and Beris, (b) Carreau-Yasuda and (c) Newtonian viscosity model.

Figure 13 plots Oscillatory Shear Index contours for the selected viscosity models. OSI contours depict the zone of shear oscillation and its intensity. In Figure 13, the OSI distributed zones in the Level 1 artery can be seen with hotspots of high and low OSI values, signifying the nature of shear stress oscillations. The region with high OSI values is more prone to a pro-inflammatory response by the endothelial cells, whereas the low value of the OSI zone indicates unidirectional shear stress; therefore, an anti-inflammatory response for the cell is obtained. As the complexity of the descending aorta gradually decreases, the OSI zones are also averaged uniformly as the geometrical features are toned down in the subsequent levels of simplification. Lastly, a uniform OSI distribution is observed in Level 3, as no geometrical disturbances are present. It is clear that the asymmetry of Level 1 is lost in both Levels 2 and 3 due to the geometric simplification.

A fair comparison of the time-averaged hemodynamic indicators across geometric levels is shown in Fig. 14 for TAWSS (Fig. 14 (a)) and OSI (Fig.14 (b))

averaged over the circumference at each axial location. As might be expected, the predictions in Level 3 are a monotonic function, while predictions in Levels 1 and 2 show oscillations due to axial variations in the geometry. For all data shown, the Level 3 predictions represent an average behavior of the oscillatory predictions obtained for Levels 1 and 2. The usefulness of Level 2 is readily visible in these results since, mostly, it closely follows the predictions of Level 1. In the present discussion, the Level 1 predictions are averaged over the circumference and the Level 2 geometry is built by averaging diameters at various axial locations. The consistency of Levels 1 and 2 is visible even more for the non-Newtonian models and shows some differences for the Newtonian fluid, especially for OSI. These results bolster the proposition that a somewhat smoother geometry (like Level 2) will be able to capture the fluctuations in hemodynamic parameters, although the local asymmetry will be lost. As discussed later in Section 3.5, this presents a valid ground for a speed-accuracy trade-off since convergence in the smoother geometries is faster and yet captures the essence of the predictions of Level 1. However, only Level 1 (patient-specific geometry) can be used without any further simplifications in applications where the details of local asymmetry are required.

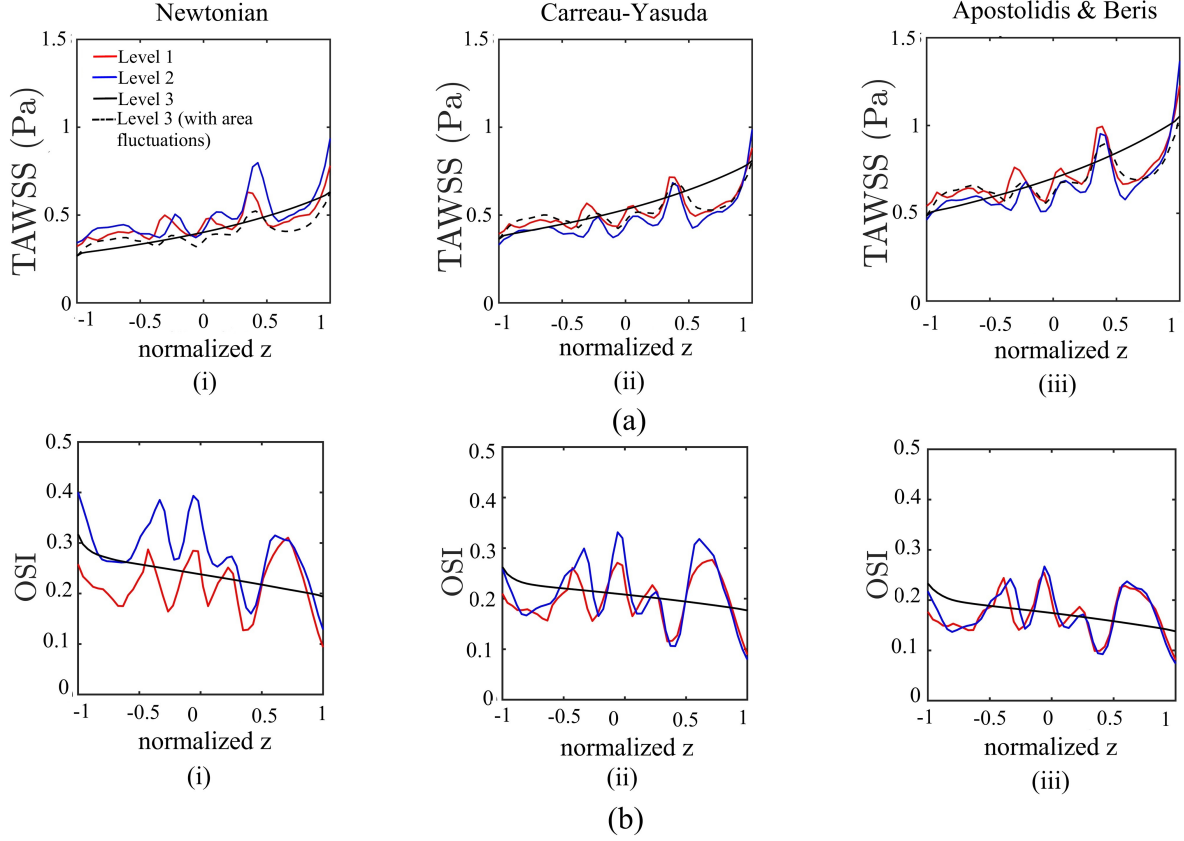


Figure 14: Comparison of TAWSS and OSI for (i) Newtonian, (ii) Carreau-Yasuda, and (iii) Apostolidis and Beris models. (a) TAWSS: Time-Averaged Wall Shear Stress. (b) OSI: Oscillatory Shear Index for the geometric simplification levels 1-3 of the descending aorta. Results of Level 1 shown here are averaged over the circumference for each axial location.

For TAWSS, Level 2 is able to provide predictions close to those of the circumferential averaged Level 1 data. However, Level 3 is only able to show a monotonic function representing an overall average trend. It lacks the oscillation and fluctuations that are caused due to area fluctuation, characteristic of Levels 1 and 2. It is possible to ask, from the prediction of TAWSS of Level 3 and knowing the area changes, is it possible to recover the prediction of Levels 1 and 2? The following approach is adopted here. Shear stress is given by

$$\text{TAWSS} \sim \mu_{app} \frac{\partial u}{\partial z}$$

for flow in a duct. In terms of the order of magnitudes, the expression can be written as

$$\text{TAWSS} \sim \mu_{app} \frac{U}{D} \frac{\partial u^*}{\partial z^*}$$

Here, symbols U and D are the characteristic velocity and diameter at any location within the duct. The average velocity at any location can be estimated by knowing the volumetric flow rate and local cross-sectional area. Since we know the total volumetric flow rate and area at any location, U and D can be estimated for local perturbations while $\frac{u^*}{z^*}$ can be assumed to be unaffected. At a high shear rate, μ_{app} can be assumed to be a limiting value (Figure 3). Thus, TAWSS can be estimated locally from the characteristic velocity and diameter at every cross-section. These estimates are shown in Figure 14(a) for all viscosity models by black dashed lines.

These results clearly indicate the success of the estimated TAWSS across all models, with non-Newtonian models performing slightly better. Thus, knowing the results of the simulation for Level 3 and the prescribed area perturbations, the realistic local TAWSS in a patient-specific geometry can be readily estimated.

3.4 Q criterion

Another critical parameter for studying strain rate and rotational characteristics is the Q criterion. It is based on the velocity gradient tensor, which is given as the summation of a symmetric and anti-symmetric part as follows:

$$\nabla \mathbf{u} = \frac{\nabla \mathbf{u} + \nabla \mathbf{u}^T}{2} + \frac{\nabla \mathbf{u} - \nabla \mathbf{u}^T}{2}$$

The first term is the symmetric part and represents the rate of strain tensor ($\bar{\bar{\gamma}}$). The second term represents the anti-symmetric part of the vorticity tensor ($\bar{\bar{\Omega}}$). The Q criterion is then calculated as:

$$Q = \frac{\|\bar{\bar{\Omega}}\| - \|\bar{\bar{\gamma}}\|}{2} \quad (14)$$

A positive Q value shows the region with a dominance of rotational flow. Similarly, a negative value denotes a zone where rotational flows are not dominant. In Figure 15a, an iso-surface of the Q -criterion is shown for $Q = 0.1$. Similarly, in Figure 15b, it is shown for $Q = -0.1$. It is clear that the simplification of the artery leads to a uniform flow distribution. Strong vortex structures are created in Level 1 and progressively disintegrate in Level 2 and Level 3.

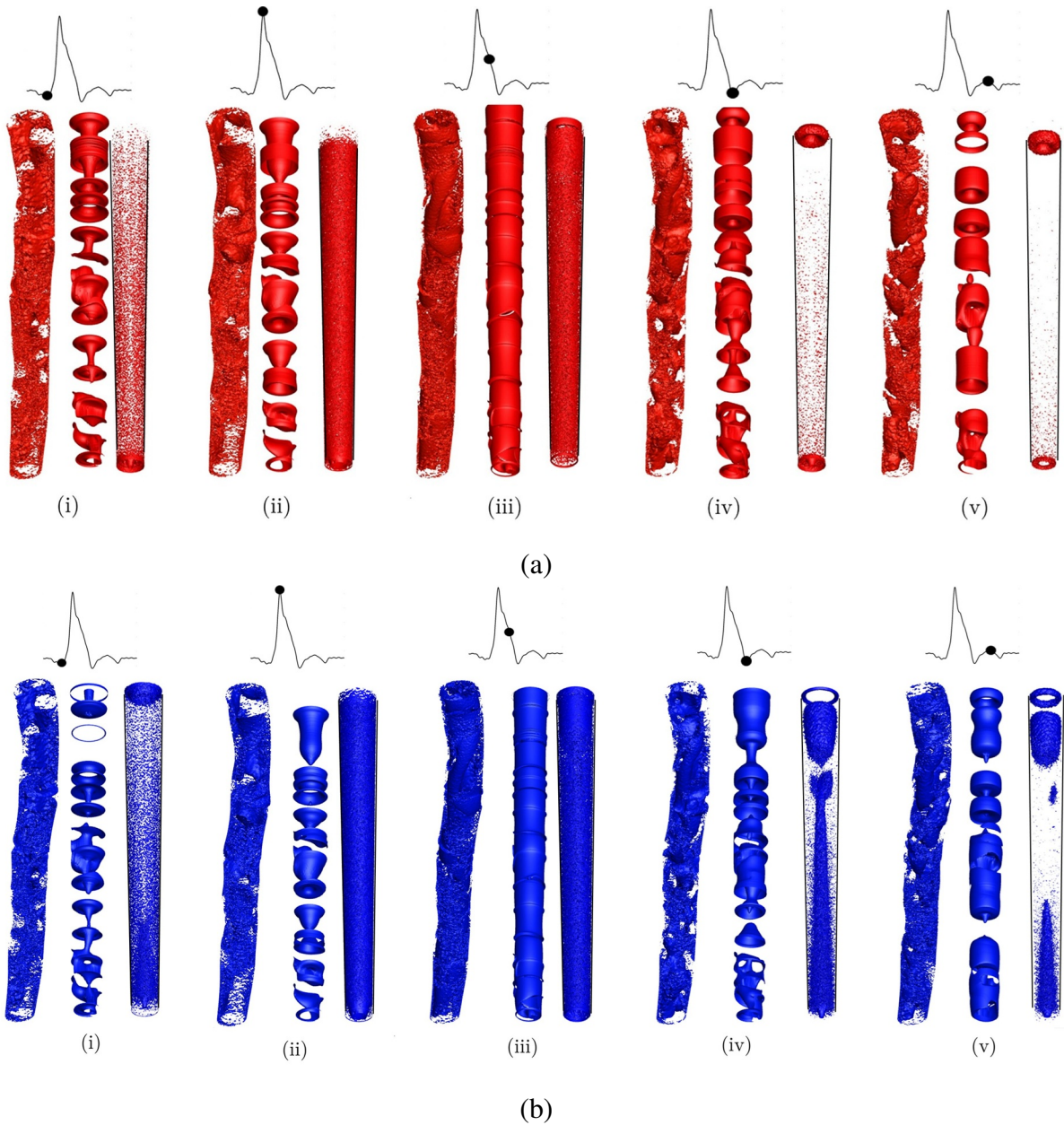


Figure 15: Iso-surfaces of the Q criterion are shown for dimensional values of (a) 0.1 and (b) - 0.1 values for the three geometries simulated with the Apostolidis and Beris viscosity model at the selected time instants of the vascular waveform. Within time instants of (i) - (v), the three levels are arranged from left to right.

In the deceleration phase, the Q function swells out, filling the tube volume. During the diastolic flow is weak, and the Q contour created in Level 3 occupies a smaller volume within the tube. Overall, vortex structure weakens considerably as the geometry is simplified. A similar trend is also seen for the contours of $Q = -0.1$, as shown in Figure 15b. The nature of the distribution of the positive values of the Q function is associated with wall shear stress, whereas negative

Q values indicate that strain dominates over rotation, signifying zones of strong deformation rather than vortex formation.

3.5 Speed Accuracy trade-off

In the preceding sections, we have shown details of the accuracy aspects arising from various simplification levels. As discussed, Level 2 mostly captures the local effects for all parameters, but the local asymmetry visible in the original Level 1 is lost. Level 3 is unable to capture any of the local effects and only shows a “representative average” of results obtained in Level 1. However, for the wall shear stress, simulation data of Level 3 can be reconstructed using scaling principles, which agree well with the detailed calculations of Level 1. Thus, each level has its own utility and is able to provide limited but useful information about the flow field. In the present section, we discuss the reduction in computational time with geometric simplification. In Level 2 geometry, we used 25 individual slices over the length of the artery, each slice being a cylindrical patch. To perform an analysis of the effect of this number, we reconstructed the entire artery by extracting the cross-sectional area of the Level 1 geometry along its length. We then developed multiple equivalent geometries consisting of 25, 20, 15, 10, and 5 slices apart from Level 3, which does not have any slices. Using a grid-independence test, we analysed all reconstructed geometries with Newtonian blood viscosity under steady flow conditions, employing a uniform inlet velocity.

In Figure 16(a), we show the friction factor for all reconstructed geometries, including the Level 1 geometry, as a function of the mesh element size. For Level 1 geometry, the converged mesh size appears to be around 0.6. Similarly, the friction factor for all other simplified geometries is plotted, with convergence occurring at about an element size of 0.8. The results indicate that the simplified geometries require coarser meshes to achieve grid convergence compared to the Level 1 geometry. This finding aligns with expectations, as the simplified geometries are symmetrical along their axis and less complex, making convergence attainable on coarser meshes. Consequently, the simplified arteries are expected to yield faster simulations than Level 1. Apart from the asymmetry,

most of the local flow aspects are resolved by the Level 2 geometry. Thus, we can perform simulations to a similar level of accuracy using a coarser mesh, thereby increasing the computational efficiency of the simulation.

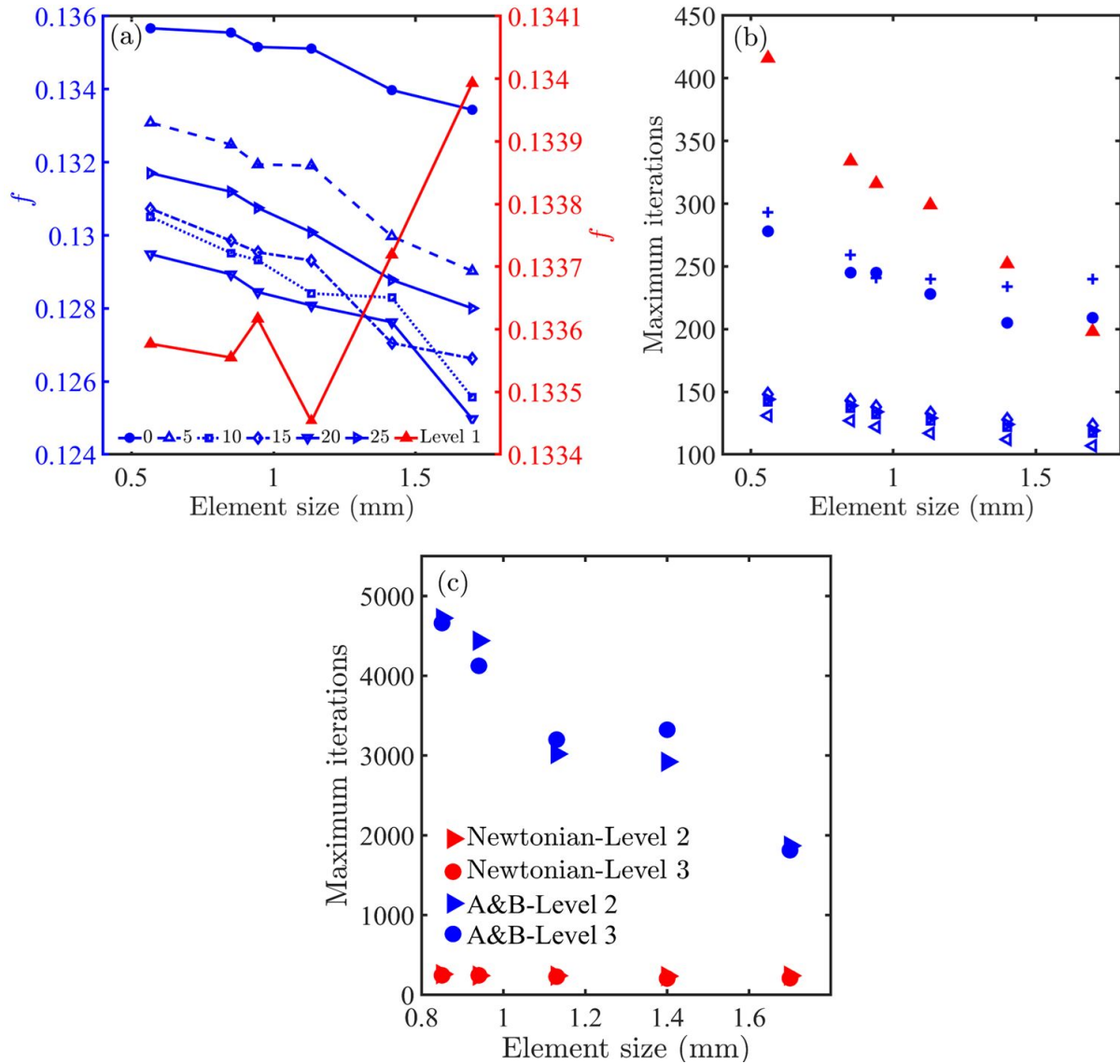


Figure 16: Speed-accuracy analysis is carried out by performing (a) grid independence test for simplified geometries up to 25 slices and comparing their respective friction factors. (b) The maximum number of iterations required to reach the tolerance of $1e-5$ in velocity is plotted as a function of the element size. (c) Maximum number of iterations is plotted for the Apostolidis and Beris (A&B) and Newtonian viscosity models for Level 2 (with 25 slices) and Level 3 simplification.

Further, to show the speed increase with geometric simplification, we show the maximum number of iterations required to reach a prescribed convergence

criterion as a function of the element size, in Figure 16(b). The data reveal that simplified geometries with 5 to 20 slices require approximately 150 iterations. In contrast, the simplified artery with 25 slices and the geometry with zero slices need around 300 iterations for the smallest element size and 200 iterations for the largest element size. For Level 1 geometry, the number of iterations increases as the element size is decreased, which is consistent with expectations for unstructured meshes over complex three-dimensional geometries. Thus, there is a clear trend of improvement in terms of the number of iterations (and thus, the speed of computations) as we move towards simplified geometric representations. The difference is as large as four times between Level 1 and Level 2 (with 25 slices) at their optimal element sizes.

In Figure 16(c), the Apostolidis and Beris viscosity model is compared with the Newtonian viscosity model with respect to the maximum number of iterations as a function of element size for Level 2 and Level 3 geometries. A significant difference is observed when the viscosity model becomes non-Newtonian. For the converged mesh, nearly 5000 iterations are required for the non-Newtonian viscosity model as compared to the Newtonian. Overall, for meshes with acceptable grid quality, geometric simplification reduces the number of iterations required, nonlinearity of the viscosity model increases the number of iterations, while grid refinement increases the number of iterations.

4 Discussion

The study provides two broad observations. First, geometric simplifications can be useful for generating fast but approximate insights, especially when time constraints exist in clinical decision-making. The approximate solutions can often be improved using suitable scale analysis. However, for a detailed analysis, retaining complete geometrical fidelity is essential. Secondly, for larger arteries, the Newtonian model can provide qualitatively similar predictions faster than the non-Newtonian ones in terms of CPU time. The findings also emphasise the importance of combining accurate hemodynamic indicators such as time-averaged wall shear stress and the Q -function with newly devel-

oped blood viscosity models for better prediction of blood-tissue interaction. These insights could aid in designing personalised treatments, evaluating surgical interventions, and improving diagnostic accuracy in detecting the onset of cardiovascular diseases.

5 Conclusions

A detailed study on a patient-specific geometry of the descending aorta with two simplified representations and three viscosity models is conducted. The geometry is extracted from CT scan data shared by a hospital and reconstructed using image processing tools. Realistic time-dependent boundary conditions are applied at the inlet and outlet in terms of pulsatile velocity (mean $Re = 313$ and peak $Re = 1687$) and outlet pressure, respectively. For the geometrical approximation, the original artery (termed Level 1) is further simplified into two more levels, denoted as Level 2 and Level 3. Level 2 is based on the cross-sections of Level 1, which is divided into 25 sections, with each part having a representative average diameter. Thus, Level 2 captures some of the undulations and area fluctuations of Level 1 but loses the local asymmetry of the original. Level 3 represents a smooth duct based on the inlet and outlet cross-sectional area of the actual artery. The 3D simulations are performed with three blood rheology models – Newtonian, Carreau-Yasuda, and Apostolidis and Beris. Various aspects of blood flow for all the levels of the descending aorta geometry (with selected blood viscosity models) are studied. The following conclusions are arrived at in the present work.

1. As the geometrical complexity is averaged out, the overall flow field becomes uniform, with a reduction in the strength of the recirculation zones near wall perturbations. For Level 1 geometry, the flow field shows a significant number of recirculation zones near the walls. Some of these zones are visible in Level 2 as well, though with reduced intensity. No such zone of reversed flow is visible in Level 3, where the flow field is practically unidirectional.
2. The simplification of the geometry affects the strain rate distribution, fur-

ther influencing the wall shear stress (WSS). Simulations show that Level 2 geometry could approximate the WSS distribution reasonably well, capturing major patterns and magnitudes while missing the local asymmetry in the stress profiles. However, Level 3 shows only a smooth variation of the WSS without showing undulations.

3. The correlation analysis indicates that Level 2 prediction of WSS maintain a strong agreement with Level 1 results, thereby preserving greater accuracy when employing non-Newtonian models. In contrast, this accuracy significantly diminishes in Levels 2 and 3 when using Newtonian viscosity. Pressure remains well-correlated except during the diastolic phases C and D for the Newtonian model.
4. The variations of the hemodynamic indicators such as TAWSS and OSI bolster these earlier assertions further. Level 2 predictions are particularly close to those obtained in Level 1, especially when both sets of data are averaged over the circumference. However, Level 3 predictions are without any fluctuations and are, at best, a representative average.
5. A simple estimate of the actual WSS in the original artery can be obtained by knowing the prediction from Level 3, scaled by the area fluctuation. The estimates thus retrieved are close to the ones obtained with Level 1.
6. The speed test showed that computations with Levels 2 and 3 could be about 4 times faster than Level 1. The Newtonian model needs about 10 times fewer iterations than the Apostolidis and Beris model for a comparable convergence level and grid refinement.

Acknowledgment

Authors acknowledge the National Supercomputing Mission (NSM) for providing computing resources of 'PARAM Sanganak' at IIT Kanpur, which is implemented by C-DAC and supported by the Ministry of Electronics and Information Technology (MeitY) and Department of Science and Technology (DST), Government of India. Also, we would like to thank the computer centre (www.iitk.ac.in/cc) at IIT Kanpur for providing the resources to carry out the reported work. The authors gratefully acknowledge the kind support provided by

the DST NSM project with DST/NSM/R&D_HPC_Applications/2021/18 sanction number .

Author Declaration

The authors have no conflicts to disclose.

References

- [1] Yiannis S Chatzizisis, Ahmet Umit Coskun, Michael Jonas, Elazer R Edelman, Charles L Feldman, and Peter H Stone. Role of endothelial shear stress in the natural history of coronary atherosclerosis and vascular remodeling: molecular, cellular, and vascular behavior. *Journal of the American College of Cardiology*, 49(25):2379–2393, 2007.
- [2] World Health Organization. Cardiovascular diseases (cvd) factsheet. <http://www.who.int/mediacentre/factsheets/fs310/en/>, 2017.
- [3] Ying-Ying Zheng, Yi-Tong Ma, Jin-Ying Zhang, and Xiang Xie. Covid-19 and the cardiovascular system. *Nature reviews cardiology*, 17(5):259–260, 2020.
- [4] Ashkan Javadzadegan, Andy SC Yong, Michael Chang, Martin KC Ng, Masud Behnia, and Leonard Kritharides. Haemodynamic assessment of human coronary arteries is affected by degree of freedom of artery movement. *Computer methods in biomechanics and biomedical engineering*, 20(3):260–272, 2017.
- [5] Thanapong Chaichana, Zhonghua Sun, and James Jewkes. Computation of hemodynamics in the left coronary artery with variable angulations. *Journal of biomechanics*, 44(10):1869–1878, 2011.
- [6] T Asakura and T Karino. Flow patterns and spatial distribution of atherosclerotic lesions in human coronary arteries. *Circulation Research*, 66(4):1045–1066, April 1990.
- [7] Adel M. Malek. Hemodynamic Shear Stress and Its Role in Atherosclerosis. *JAMA*, 282(21):2035, December 1999.
- [8] D N Ku, D P Giddens, C K Zarins, and S Glagov. Pulsatile flow and atherosclerosis in the human carotid bifurcation. Positive correlation between plaque location and low oscillating shear stress. *Arteriosclerosis: An Official Journal of the American Heart Association, Inc.*, 5(3):293–302, May 1985.

- [9] Peter H. Stone, Ahmet U. Coskun, Scott Kinlay, Maureen E. Clark, Milan Sonka, Andreas Wahle, Olusegun J. Ilegbusi, Yerem Yeghiazarians, Jeffrey J. Popma, John Orav, Richard E. Kuntz, and Charles L. Feldman. Effect of Endothelial Shear Stress on the Progression of Coronary Artery Disease, Vascular Remodeling, and In-Stent Restenosis in Humans: In Vivo 6-Month Follow-Up Study. *Circulation*, 108(4):438–444, July 2003.
- [10] C.A. Taylor and C.A. Figueroa. Patient-Specific Modeling of Cardiovascular Mechanics. *Annual Review of Biomedical Engineering*, 11(1):109–134, August 2009.
- [11] Kyung Eun Lee, Sung Woong Shin, Gook Tae Kim, Jin Ho Choi, and Eun Bo Shim. Prediction of Plaque Progression in Coronary Arteries Based on a Novel Hemodynamic Index Calculated From Virtual Stenosis Method. *Frontiers in Physiology*, 10:400, May 2019.
- [12] Joseph Knight, Ufuk Olgac, Stefan C. Saur, Dimos Poulikakos, William Marshall, Philippe C. Cattin, Hatem Alkadhi, and Vartan Kurtcuoglu. Choosing the optimal wall shear parameter for the prediction of plaque location—A patient-specific computational study in human right coronary arteries. *Atherosclerosis*, 211(2):445–450, August 2010.
- [13] Sumith Yesudasan and Rodney D. Averett. Recent advances in computational modeling of fibrin clot formation: A review. *Computational Biology and Chemistry*, 83:107148, December 2019.
- [14] Chen Peng, Wei He, Jingyang Luan, Tong Yuan, Weiguo Fu, Yun Shi, and Shengzhang Wang. Preliminary establishment and validation of the inversion method for growth and remodeling parameters of patient-specific abdominal aortic aneurysm. *Biomechanics and Modeling in Mechanobiology*, 23(4):1137–1148, 2024.
- [15] Salvatore Cito, Marco Domenico Mazzeo, and Lina Badimon. A Review of Macroscopic Thrombus Modeling Methods. *Thrombosis Research*, 131(2):116–124, February 2013.

- [16] Parham Eshtehardi, Michael C. McDaniel, Jin Suo, Saurabh S. Dhawan, Lucas H. Timmins, José Nilo G. Binongo, Lucas J. Golub, Michel T. Corban, Alope V. Finn, John N. Oshinsk, Arshed A. Quyyumi, Don P. Giddens, and Habib Samady. Association of Coronary Wall Shear Stress With Atherosclerotic Plaque Burden, Composition, and Distribution in Patients With Coronary Artery Disease. *Journal of the American Heart Association*, 1(4):e002543, August 2012.
- [17] Alireza Gholipour, Mergen H. Ghayesh, Anthony Zander, and Rajiv Mahajan. Three-dimensional biomechanics of coronary arteries. *International Journal of Engineering Science*, 130:93–114, September 2018.
- [18] Alireza Karimi, Mahdi Navidbakhsh, Shahab Faghihi, Ahmad Shojaei, and Kamran Hassani. A finite element investigation on plaque vulnerability in realistic healthy and atherosclerotic human coronary arteries. *Proceedings of the Institution of Mechanical Engineers, Part H: Journal of Engineering in Medicine*, 227(2):148–161, February 2013.
- [19] Jessica Benitez Mendieta, Davide Fontanarosa, Jiaqiu Wang, Phani Kumari Paritala, Tim McGahan, Thomas Lloyd, and Zhiyong Li. The importance of blood rheology in patient-specific computational fluid dynamics simulation of stenotic carotid arteries. *Biomechanics and modeling in mechanobiology*, 19:1477–1490, 2020.
- [20] Lili Niu, Ming Qian, Wei Yang, Long Meng, Yang Xiao, Kelvin K. L. Wong, Derek Abbott, Xin Liu, and Hairong Zheng. Surface Roughness Detection of Arteries via Texture Analysis of Ultrasound Images for Early Diagnosis of Atherosclerosis. *PLoS ONE*, 8(10):e76880, October 2013.
- [21] Arno Schmidt-Trucksäss, Markus Sandrock, Da-chuan Cheng, Hans-Michael Müller, Manfred W Baumstark, Rainer Rauramaa, Aloys Berg, and Martin Huonker. Quantitative measurement of carotid intima-media roughness—effect of age and manifest coronary artery disease. *Atherosclerosis*, 166(1):57–65, January 2003.

- [22] M Cinthio, H Hasegawa, and H Kanai. Initial phantom validation of minute roughness measurement using phase tracking for arterial wall diagnosis non-invasively in vivo. *IEEE Transactions on Ultrasonics, Ferroelectrics and Frequency Control*, 58(4):853–857, April 2011.
- [23] Jie Yi, Fang-Bao Tian, Anne Simmons, and Tracie Barber. Impact of modelling surface roughness in an arterial stenosis. *Fluids*, 7(5):179, 2022.
- [24] R Shukla, SS Bhatt, A Medhavi, and R Kumar. Effect of surface roughness during peristaltic movement in a nonuniform channel. *Mathematical Problems in Engineering*, 2020(1):9643425, 2020.
- [25] David G Owen, Torsten Schenkel, Duncan ET Shepherd, and Daniel M Espino. Assessment of surface roughness and blood rheology on local coronary haemodynamics: a multi-scale computational fluid dynamics study. *Journal of the Royal Society Interface*, 17(169):20200327, 2020.
- [26] Adam Updegrave, Nathan M Wilson, Jameson Merkow, Hongzhi Lan, Alison L Marsden, and Shawn C Shadden. Simvascular: an open source pipeline for cardiovascular simulation. *Annals of biomedical engineering*, 45:525–541, 2017.
- [27] C. J. Mills, I. T. Gabe, J. H. Gault, D. T. Mason, Jr. Ross, J., E. Braunwald, and J. P. Shillingford. Pressure-flow relationships and vascular impedance in man. *Cardiovascular Research*, 4(4):405–417, 10 1970.
- [28] EDWARD W Merrill and GERARD A Pelletier. Viscosity of human blood: transition from newtonian to non-newtonian. *Journal of applied physiology*, 23(2):178–182, 1967.
- [29] Young I Cho and Kenneth R Kensey. Effects of the non-newtonian viscosity of blood on flows in a diseased arterial vessel. part 1: Steady flows. *Biorheology*, 28(3-4):241–262, 1991.
- [30] Alex J Apostolidis and Antony N Beris. Modeling of the blood rheology in steady-state shear flows. *Journal of Rheology*, 58(3):607–633, 2014.

- [31] Ryan M Miller and Jeffrey F Morris. Normal stress-driven migration and axial development in pressure-driven flow of concentrated suspensions. *Journal of non-newtonian fluid mechanics*, 135(2-3):149–165, 2006.
- [32] Mahesh S Nagargoje, Deepak K Mishra, and Raghvendra Gupta. Pulsatile flow dynamics in symmetric and asymmetric bifurcating vessels. *Physics of Fluids*, 33(7), 2021.
- [33] Frank Gijsen, Yuki Katagiri, Peter Barlis, Christos Bourantas, Carlos Collet, Umit Coskun, Joost Daemen, Jouke Dijkstra, Elazer Edelman, Paul Evans, et al. Expert recommendations on the assessment of wall shear stress in human coronary arteries: existing methodologies, technical considerations, and clinical applications. *European heart journal*, 40(41):3421–3433, 2019.
- [34] David N Ku and Don P Giddens. Pulsatile flow in a model carotid bifurcation. *Arteriosclerosis: An Official Journal of the American Heart Association, Inc.*, 3(1):31–39, 1983.